nature communications

Article

https://doi.org/10.1038/s41467-025-56806-w

Doping dependence of the dipolar correlation length scale in metallic $SrTiO_3$

Received: 5 April 2024

Accepted: 30 January 2025

Published online: 07 March 2025

Check for updates

Benoît Fauqué[1] ✉, Shan Jiang[1], Tom Fennell[2], Bertrand Roessli[2], Alexandre Ivanov[3], Celine Roux-Byl[4], Benoît Baptiste[5], Philippe Bourges[6], Kamran Behnia[4] & Yasuhide Tomioka[7]

Superconducting domes, ubiquitous across a variety of quantum materials, are often understood as a window in which pairing is favored, opened by the fluctuations of competing orders. Yet, the understanding of how such a window closes is missing. Here, we show that inelastic neutron scattering, by quantifying a length scale associated with the dipoles correlation, ℓ_0, addresses this issue. We find that, within the experimental precision, the end of the superconducting dome coincides with the end of a highly polarizable state (in which ℓ_0 is longer than the interatomic distance). Thus, the superconducting dome is driven by the competition between the increase in the density of states and the inevitable collapse of the quantum paraelectric phase. This is compatible with a crucial role played by the soft ferroelectric mode in driving superconductivity. Such a scenario may also be at work in other quantum paraelectric materials, either bulk or at interfaces.

In many superconducting materials such as cuprates[1], pnictides[2], heavy fermions[3], doped band insulators[4], and oxide[5] or graphene[6] heterostructures, the superconducting transition temperature (T_c) displays a dome shape as a function of the doping. Identifying the mechanisms giving rise to these domes is the subject of intense debates.

Among superconducting domes, the case of doped $SrTiO_3$ is unique (see refs. 7,8 for reviews). In bulk crystals, the superconducting dome starts at a carrier concentration as low as $n \simeq 5 \times 10^{17}\,cm^{-3}$ for oxygen reduced samples[9,10], spans over more than three orders of magnitude and ends at $n \simeq 10^{21}\,cm^{-3}$, irrespective of the dopant identity[11,12]. This corresponds to a doping level of about 5%, an extremely low doping level compared with the threshold of superconductivity in many other materials. Moreover, by contrast with other families, the parent compound is not magnetic but is an incipient ferroelectric, the so-called *quantum paraelectric* phase. This state, characterized by a large dielectric constant $\epsilon \approx 2 \times 10^4$[13], is driven by the softening of the zone centered transverse optical (TO) phonon mode that hybridizes with the transverse acoustic (TA) phonon mode at low temperature[14–17].

Recently, it has been suggested that the coupling of electrons with ferroelectric fluctuations can lead to superconducting pairing, in particular down to a very low carrier density. This coupling can take either the form of quadratic coupling[18–20] or the form of a Rashba type electron-TO mode coupling[10,21,22]. In these theories, the attractive pairing mechanism is static with an amplitude set by k_F, the Fermi wave-vector and ℓ_0, the dipolar correlation length. ℓ_0 is given by the TO dispersion energy (E) satisfying in the parent compound[14,15] :

$$E^2(q) = \omega_{TO}^2[1 + \ell_0^2 q^2] \quad (1)$$

where $\ell_0 = \frac{v_{TO}}{\omega_{TO}}$ with ω_{TO} and v_{TO} the energy and velocity of the TO mode at the zone center. In doped polar materials, ℓ_0 represents the radius of local electric dipoles formed around defects[23,24]. In highly polarizable crystals, such as quantum paraelectrics, ℓ_0 can extend remarkably,

[1]JEIP (USR 3573 CNRS), Collège de France, Paris, France. [2]PSI Center for Neutron and Muon Sciences, Villigen, Switzerland. [3]Intitut Laue Langevin, Grenoble, France. [4]Laboratoire de Physique et d'Etude de Matériaux (CNRS) ESPCI Paris, Université PSL, Paris, France. [5]IMPMC-Sorbonne Université and CNRS, Paris, France. [6]Laboratoire Léon Brillouin, CEA-CNRS, Université Paris-Saclay, Gif-sur-Yvette, France. [7]National Institute of Advanced Industrial Science and Technology (AIST), Tsukuba, Japan. ✉e-mail: benoit.fauque@espci.fr

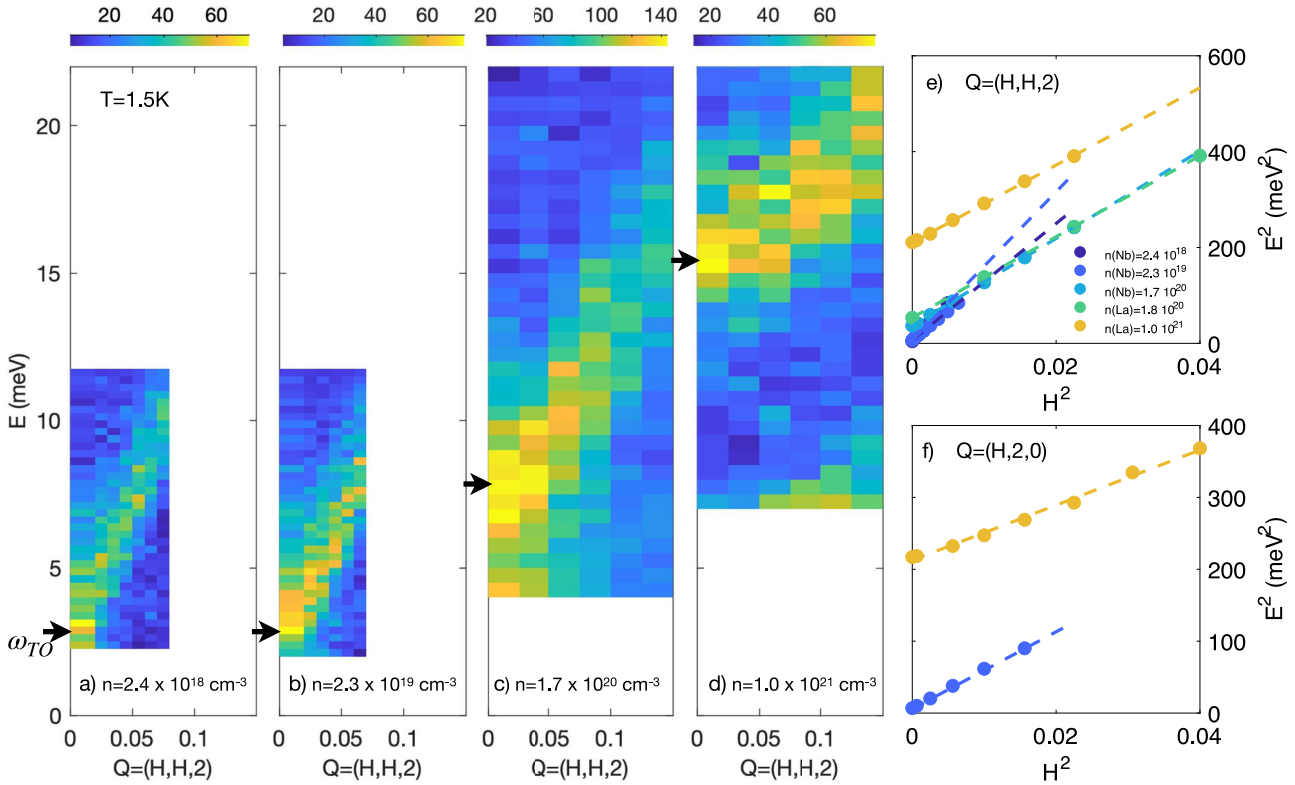

Fig. 1 | Doping evolution of the soft ferroelectric mode dispersion at T = 1.5 K. Momentum-and energy-resolved neutron scattering intensity map of along the (H,H,2) direction in $SrTi_{1-x}Nb_xO_3$ with an electron density **a** n(Nb) = 2.4×10^{18} cm^{-3}, **b** n(Nb) = 2.3×10^{19} cm^{-3}, **c** n(Nb) = 1.8×10^{20} cm^{-3} and in $Sr_{1-x}La_xTiO_3$ with **d** n(La) = 1.0×10^{21} cm^{-3} at T = 1.5 K. **e** Dispersion of the soft ferroelectric mode along [H,H,0] for the five dopings studied as function of H². **f** same as (**e**) along [H,0,0]. For all the doping the dispersion can be fitted through : $E^2(q)=\omega_{TO}^2+v_{TO}^2q^2$, where q[1,1,0]=$\frac{2\pi}{a}\sqrt{2}$H and q[1,0,0]=$\frac{2\pi}{a}$H where a is the lattice parameter of $SrTiO_3$, that allows one to determine $\ell_0 = \frac{v_{TO}}{\omega_{TO}}$. Black arrows on (**a**–**d**) indicate the position of ω_{TO}.

reaching a few nanometers. Defects cooperate via dipolar interactions over long distances to generate mesoscopic dipoles. This cooperative behavior can lead to the percolation of dipoles and induce a ferroelectric ground state, as observed in $Sr_{1-x}Ca_xTiO_3$[24].

Here, we present the first systematic study of the dispersion of the soft ferroelectric phonon mode in electron doped $SrTi_{1-x}Nb_xO_3$ and $Sr_{1-x}La_xTiO_3$. Using inelastic neutron scattering (INS), a probe that allows to determine ℓ_0, we track its decrease with electron doping as a result of the hardening of the TO-mode, the decrease of the velocity of the TO mode, and the breakdown of the TO/TA hybridization. Comparing ℓ_0 and k_F leads to a qualitative picture of the superconducting dome of $SrTiO_3$. The increase in carrier density has opposite consequences for k_F and for ℓ_0. The former increases, while the latter decreases. When carrier density attains a threshold value ($\simeq 10^{21}$ cm^{-3}), ℓ_0 saturates to a value comparable to the interatomic distance and concomitantly, superconductivity disappears. Thus, the superconducting dome coincides with a crossover regime where the highly polarizable dielectric state of undoped $SrTiO_3$ is tuned into a normal dielectric state through electron doping. Our result provides direct evidence of the key role of the soft TO mode and its hybridization with the TA mode in the superconducting dome of quantum paraelectrics.

Results

Figure 1a–d show the dispersion of the soft ferroelectric mode as measured by INS along the (H,H,0) direction for carrier densities ranging from 2.4×10^{18} cm^{-3} to 1.0×10^{21} cm^{-3} at T = 1.5 K. The identity of the dopants (La or Nb) is indicated in parentheses for each carrier density. Descriptions of the samples, their characterization by electrical transport measurement and the configuration of spectrometers are given in the Supplementary Information Note A. Convolution of the phonon spectral function with the spectrometer resolution function allows accurate fits and independent determination of ω_{TO}, v_{TO} and the energy width of the TO-mode (Γ), see Supplementary Information Note B. In the whole doping range, the energy dispersion of the TO mode satisfies Eq.(1) along both directions (H,H,2) and (H,2,0), see Fig. 1e, f.

Figure 2a shows the energy scans at **Q** = (0,0,2) for five of the samples studied at T = 1.5 K. The soft TO mode begins to harden when the carrier density exceeds 2.3×10^{19} cm^{-3}. Figure 2b–d show the deduced doping evolution of ω_{TO}, v_{TO} and Γ. As doping increases, ω_{TO} increases from 2.1 meV at n(Nb) = 2.4×10^{18} cm^{-3}, which is comparable to the value in pure $SrTiO_3$, to 17.0 meV at n(La) = 1.6×10^{21} cm^{-3}. This sudden hardening of the TO mode is accompanied by a slight decrease of v_{TO} at low temperature of about 40%, and a slight decrease of its energy width. Like in pure $SrTiO_3$[14,15], we note no anisotropy in the TO-dispersion across the doping range studied (v_{TO}(**Q**//[1, 1, 0]) ≈ v_{TO}(**Q**//[1, 0, 0])).

The collapse of the quantum para-electric regime upon doping is further supported by the temperature dependence of ω_{TO} and v_{TO} shown on Fig. 3a, b. Up to n(Nb) = 2.3×10^{19}cm^{-3}, the T-dependence of ω_{TO} and v_{TO} shows almost no difference from the parent compound[14] (black open square points in Fig. 3a, b). Above this concentration, the TO mode becomes almost temperature independent. Similar results have also been observed in oxygen reduced samples (see Supplementary Information Note B). At the highest doping studied, the system is no longer in the quantum para-electric phase. v_{TO}, by contrast, barely changes with temperature, and decreases by 40% with doping.

Previous studies documented hybridization between the TO and TA branches in the undoped $SrTiO_3$[14,15,17]. This hybridization, a consequence of the anharmonic coupling of phonon modes[16], is

https://doi.org/10.1038/s41467-025-56806-w

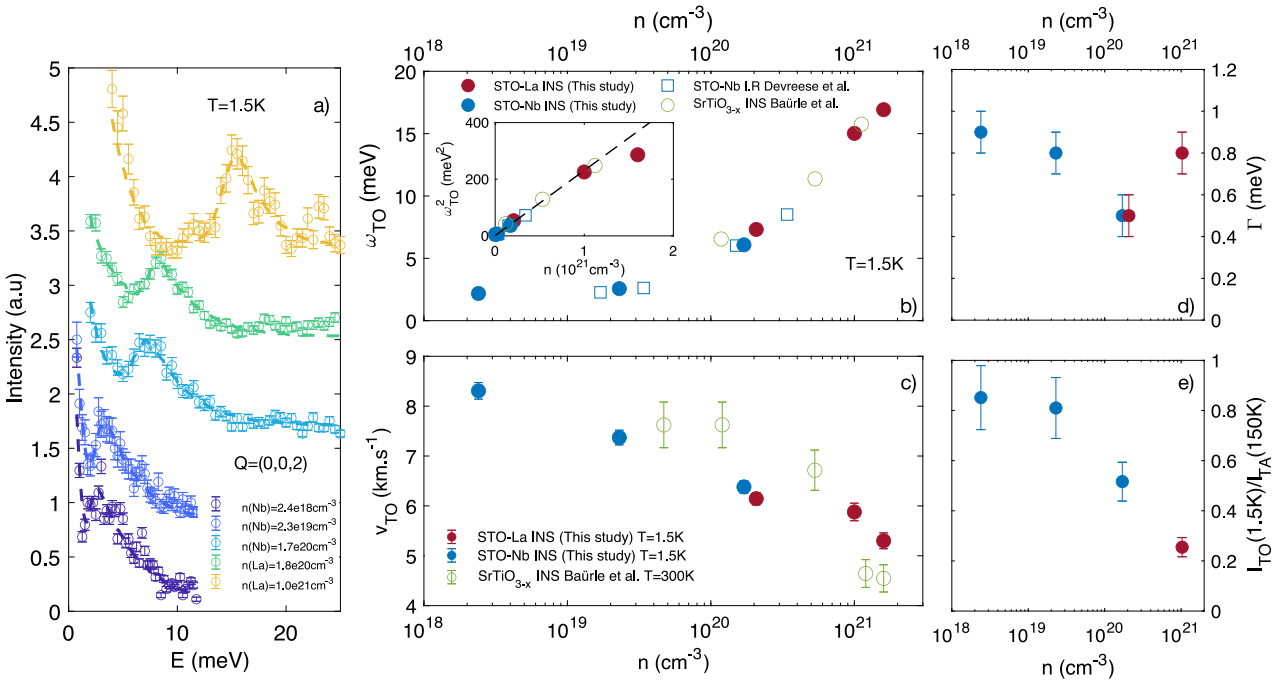

Fig. 2 | Doping evolution of the soft ferroelectric mode properties at T = 1.5 K. **a** E-scans at **Q** = (0, 0, 2) for five electron doped samples. Curves are shifted for clarity. **b** ω_{TO}*vs.n* in linear-log scale in oxygen reduced STO (green points from ref. 30), in Nb-doped STO (close circle points are INS data, open squares are from infrared measurements from ref. 29), in La-doped STO (close red circles). Inset : ω_{TO}^2*vs.n* in linear scale. The dot line is a linear fit of slope 2.3×10^{19} meV².cm³. **c** v_{TO}*vs.n* in linear-log scale in Nb and La doped STO deduced from the fit of the dispersion shown in Fig. 1, in oxygen reduced samples (green open symbols) at $T = 300$ K measured along [111] direction from ref. 30. **d** Energy width (Γ_{TO}) of the TO mode at $T = 1.5$ K at H=K=0 (closed symbols). **e** Intensity of the TO mode normalized with the TA mode intensity at $T = 150$ K. Error bars are deduced from the convolution with refinement program that finds the best least-squares fit of the dispersion parameters (see Supplementary Information Note B).

concomitant with the softening of the TO mode. It manifests itself in two ways. First, there is a dramatic transfer of intensity from the TA branch towards the TO mode at **Q** = (0,0,2)[14,16]. Second, the TA mode itself softens at a finite wave-vector[17]. The latter feature has been recently ascribed to a flexo-electric effect[25]. According to our results, doping not only hardens the TO mode, but also weakens the TO-TA hybridization. When doping increases, the absolute intensity of the TO mode, normalized by the amplitude of the TA mode at high temperature in each sample decreases by about a factor four, see Fig. 2e and Supplementary Information Note B. Simultaneously, the TA softening, measured at **Q** = (0.05,0.05,2), decreases and vanishes at the highest doping (see Fig. 1c). Thus, the hardening of the TO mode is accompanied by the weakening of its coupling with the TA mode. As a result, the spectral weight transfer and the softening of the TA mode both eventually vanish with doping, thus Γ decreases. At the highest doping, we note an increase of Γ possibly related to the damping of the TO mode by the electrons, which has been proposed to explain the increase of superconductivity in ferroelectric-type materials[26,27]. The breakdown of the quantum para-electric regime is thus concomitant with the breakdown of the TO-TA hybridization, providing further evidence that both effects are intimately related.

Discussion

Our measurement allows us to quantify for the first time the doping evolution of $\ell_0 = \frac{v_{TO}}{\omega_{TO}}$, (see Fig. 4a). Due to the combined change of ω_{TO} and v_{TO}, ℓ_0 decreases by more than one order of magnitude with the doping, and saturates to the Ti-O distance ($\frac{a}{2}$, where a is the lattice parameter), above $n \approx 1 \times 10^{21}$ cm^{-3}. The comparison of the doping evolution of ℓ_0 with T_c is clue to understand the origin of the superconducting dome of $SrTiO_3$. Figure 4c shows the superconducting domes for $SrTi_{1-x}Nb_xO_3$, $Sr_{1-x}La_xTiO_3$[12] and $SrTi(^{18}O_y^{16}O_{1-y})_{3-\delta}$[28]. Regardless of the nature of the dopants, all the domes end at a carrier density of $n \approx 1 \times 10^{21}$ cm^{-3}. The end of the superconducting domes is thus concomitant with the saturation of $\ell_0 \approx \frac{a}{2}$, i.e., the end of the quantum-para-electric regime. We note that our doping evolution of ω_{TO} is in good agreement with early infra-red measurements[29] in $SrTi_{1-x}Nb_xO_3$ and INS measurements in oxygen reduced $SrTiO_3$[30]. We used this earlier data and estimated ℓ_0 in $SrTiO_{3-x}$, as shown in Fig. 4a, based on the observed temperature independence of v_{TO} in Nb and La-doped samples.

The key role of ℓ_0 in shaping the superconducting dome of $SrTiO_3$ is further highlighted once it is compared with the density of the states length scale, k_F. For Nb and La doped samples the evolution of the Fermi surface is well captured by the rigid band approximation[31,32]. It consists of three non-parabolic bands located at the Γ-point, which are successfully filled at two critical dopings: $n_{c1} = 1.2 \times 10^{18}$ cm^{-3} and $n_{c2} = 2.2 \times 10^{19}$ cm^{-3}. Figure 4b shows the doping evolution of the average Fermi momentum, k_F^i, in the three sub-bands (i = 1,2,3) as determined by the frequency of quantum oscillation studies[33] for a magnetic field parallel to the [001] direction. When the carrier density increases, k_F^i increases, while ℓ_0 decreases. As a result, $k_F^i \ell_0$ displays a dome shape whose peak shifts to a higher concentration as each sub-band fills, see Fig. 4d. For the last two bands, the peaks in $k_f^i \ell_0$ occur at approximately 3×10^{19} cm^{-3}, which is three times lower than the peak of the superconducting dome in Nb-doped $SrTiO_3$. Interestingly, for the last band, the peak occurs at $n = 5 \times 10^{19}$ cm^{-3}, close to the middle of the superconducting dome of $SrTi_{1-x}Nb_xO_3$, see Fig. 4c.

This comparison allows us to draw a qualitative picture of the doping evolution of T_c, sketched in Fig. 4c. At low doping, where

https://doi.org/10.1038/s41467-025-56806-w

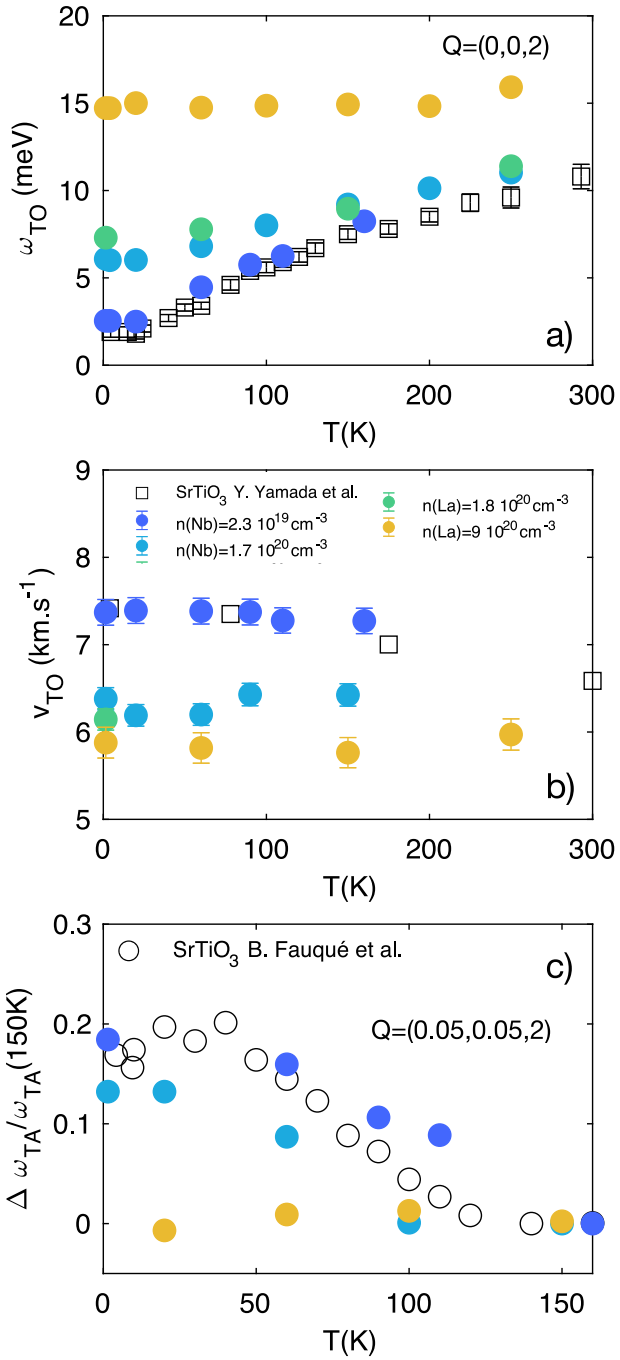

Fig. 3 | Temperature dependence of the soft ferroelectric mode. **a**, **b** Temperature dependence of ω_{TO} and v_{TO} for the five doping studied compare with the parent compound values from ref. 14 (in black open square points). **c** Amplitude of the TA softening at **Q** = (0.05,0.05,2) versus temperature for three dopings compare with the parent compound behavior (in black open circle points from ref. 17). As the TO mode becomes harder the TA softening vanishes as a consequence of the decrease of the coupling between both modes. Error bars are deduced from the convolution with refinement program that finds the best least-squares fit of the dispersion parameters (see Supplementary Information Note B).

$\ell_0 \approx 3$ nm, T_c increases due to the increase of k_F^i up to $n \approx 2 \times 10^{19}$ cm^{-3} where ℓ_0 starts to decrease. A close inspection of the behavior of T_c and ℓ_0 in the overdoped regime shows that ℓ_0 drops faster than T_c, see Fig. 4f. Above the summit of the superconducting dome, the increase in the density of states does not enhance the critical temperature. Superconductivity is weakened as ℓ_0 shrinks. Above $n \approx 0.5 \times 10^{21}$ cm^{-3}, T_c inevitably vanishes as ℓ_0 reaches its minimum value—the Ti-O distance ($\frac{a}{2}$)—at which point the normal dielectric state is fully reached.

So far, the overdoped regime has been understood as the passage from the clean to the dirty limit[34], and the end of the dome as the end of the anti-adiabatic regime[10]. Indeed, the ratio of $\frac{E_F}{\omega_{TO}}$ remains approximately constant at 3–4, placing it in an intermediate regime between the adiabatic ($E_F \gg \omega_{TO}$) and anti-adiabatic ($E_F \ll \omega_{TO}$) limits. Our result identifies the length scale ℓ_0, which drives the decrease of T_c and of the superconducting gap, Δ, whose ratio has been found constant to the weak-coupling BCS value across the dome[10,35]. This result is consistent with quantum critical theories applied to ferroelectrics[36–38] and with theoretical works where electrons are coupled with the soft TO-mode[18–22,39,40]. Combined with the known Fermi surface probed by quantum oscillations studies[9,31,32,41], our result provides the parameters to quantitatively test theories of superconductivity in $SrTiO_3$. It also helps to understand the electron doping evolution of the unusual thermal conductivity[42], isotropic magneto-resistance[43] and T^2-term resistivity[44,45] in doped $SrTiO_3$.

In contrast to the overdoped regime, the underdoped regime shows a dopant dependence, see Fig. 4c. It can arise from variations in the Fermi surfaces, as evidenced in oxygen-reduced and Nb-doped $SrTiO_3$, where different Fermi seas have been found by quantum oscillation measurements[32]. It can also be attributed to a dopant-variation of ℓ_0. Under Ca, Ba or O[18] substitution, $SrTiO_3$ becomes ferroelectric. That ferroelectric state vanishes under electron doping[12,28,46]. Investigating the electron doping dependence of ℓ_0 and of the TO/TA hybridization for these ferroelectrics or in plastic deformed $SrTiO_3$[47] is an appealing perspective to elucidate the differences in their underdoped regime.

In conclusion, we show that the end of the superconducting dome of bulk $SrTiO_3$ is concomitant with the collapse of the quantum para-electric regime. This result demonstrates the key role of the soft TO mode and its hybridization with the TA branch in the superconductivity of quantum paraelectrics and their interface.

Methods

Nb-doped samples have been provided by CrysTec GmbH. La-doped samples have be grown using the floating zone technique[12]. Hall carrier densities and electron mobilities were determined using electrical transport measurements conducted with a standard four-probe method in a Quantum Design Physical Property Measurement System, up to 12 T. For further details, see Supplementary Information Note A. Inelastic neutron scattering (INS) measurements were performed on the thermal neutron triple-axis spectrometers EIGER[48] at the Swiss spallation neutron source (SINQ), Paul Scherrer Institute (PSI), Villigen, Switzerland, and IN8 at the Institut Laue-Langevin (ILL)[49], Grenoble, France, as well as on the cold triple-axis spectrometer TASP (SINQ-PSI)[50]. The samples were successively oriented such that momentum transfers **Q** of the form (H,H,L), (H,K,0) were accessible. Measurements on EIGER and IN8 were done with $k_f = 2.662$ Å^{-1} and on TASP with $k_f = 1.97$ Å^{-1} with one PG filter inserted into the scattered beam in order to eliminate higher order contamination. Except for measurements on IN8, which employed a doubly focused Si(111) monochromator, PG002 monochromators and analyzers were used. No collimations were applied. For details on the experimental fitting, see Supplementary Information Note B.

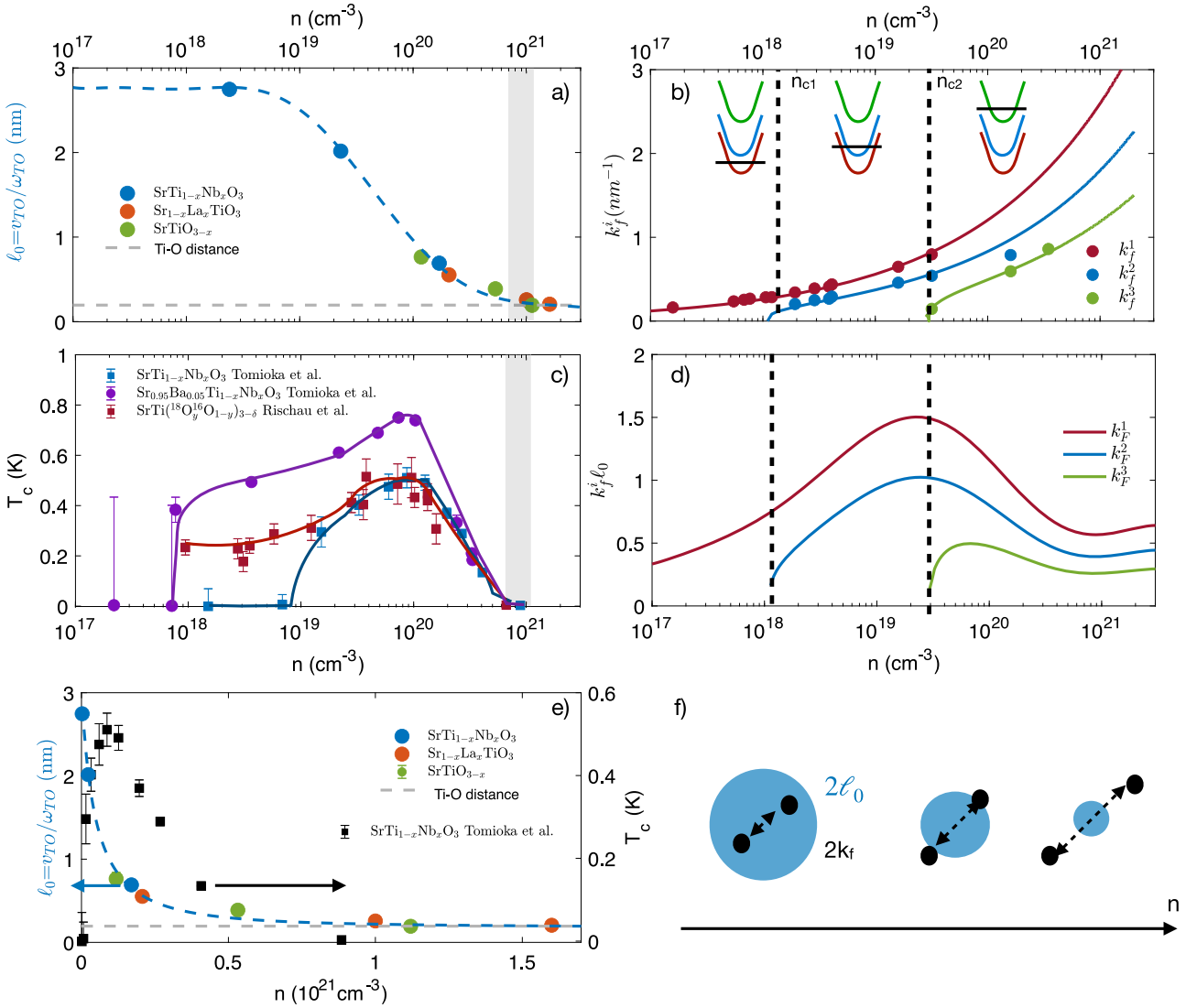

Fig. 4 | ℓ_0, T_c and k_F. **a** Doping evolution of $\ell_0=\frac{v_{TO}}{\omega_{TO}}$ for Nb-doped (blue points), La-doped (red points), reduced $SrTiO_3$ (in green points estimated from ref. 30, see the text) and $\frac{a}{2}$ (in gray dot line) where $a = 3.9$ Å is the lattice parameter of $SrTiO_3$. **b** Doping evolution of the Fermi momentum (k_F) in the three sub-bands $i = 1,2$ and 3. **c** Doping evolution of the superconducting critical temperature (Tc) according to[11,12,46]. The gray areas in (**a**, **c**) mark the end of the superconducting dome concomitant with the saturation of ℓ_0 to about $\frac{a}{2}$. **d** $k_F^i \ell_0 vs.n$ for each sub-band. **e** Comparison of the carrier dependence of ℓ_0 and T_c in linear scale. **f** Sketch of the electron doping evolution of $2\ell_0$ (blue disk) and $2k_F$ (black dot arrows). With electron doping ℓ_0 decreases and saturates to about $\frac{a}{2}$, the Ti-O distance, while k_F increases. The summit of the superconducting dome occurs when $k_F^3\ell_0$ is the largest, see the text. Error bars on T_c are from[11,12,46].

Data availability

Data collected on IN8 at ILL are available at https://doi.org/10.5291/ILL-DATA.DIR-318. All the other data supporting the findings of this study are available from the corresponding author B.F. upon request.

References

1. Keimer, B., Kivelson, S. A., Norman, M. R., Uchida, S. & Zaanen, J. From quantum matter to high-temperature superconductivity in copper oxides. *Nature* **518**, 179 (2015).
2. Fernandes, R. M. et al. Iron pnictides and chalcogenides: a new paradigm for superconductivity. *Nature* **601**, 35 (2022).
3. White, B., Thompson, J. & Maple, M. Unconventional superconductivity in heavy-fermion compounds. *Phys. C. Supercond. Appl.* **514**, 246 (2015).
4. Bustarret, E. Superconductivity in doped semiconductors. *Phys. C. Supercond. Appl.* **514**, 36 (2015).
5. Zubko, P., Gariglio, S., Gabay, M., Ghosez, P. & Triscone, J.-M. Interface physics in complex oxide heterostructures. *Annu. Rev. Condens. Matter Phys.* **2**, 141 (2011).
6. Balents, L., Dean, C. R., Efetov, D. K. & Young, A. F. Superconductivity and strong correlations in moiré flat bands. *Nat. Phys.* **16**, 725 (2020).
7. Collignon, C., Lin, X., Rischau, C. W., Fauqué, B. & Behnia, K. Metallicity and superconductivity in doped strontium titanate. *Annu. Rev. Condens. Matter Phys.* **10**, 25 (2019).
8. Gastiasoro, M. N., Ruhman, J. & Fernandes, R. M. Superconductivity in dilute $SrTiO_3$: a review. *Annl. Phys.* **417**, 168107 (2020).
9. Lin, X., Zhu, Z., Fauqué, B. & Behnia, K. Fermi surface of the most dilute superconductor. *Phys. Rev. X* **3**, 021002 (2013).
10. Yoon, H. et al. Low-density superconductivity in $SrTiO_3$ bounded by the adiabatic criterion. arXiv e-prints, arXiv:2106.10802 (2021).

11. Tomioka, Y., Shirakawa, N., Shibuya, K. & Inoue, I. H. Enhanced superconductivity close to a non-magnetic quantum critical point in electron-doped strontium titanate. *Nat. Commun.* **10**, 738 (2019).
12. Tomioka, Y., Shirakawa, N. & Inoue, I. H. Superconductivity enhancement in polar metal regions of $Sr_{0.95}Ba_{0.05}TiO_3$ and $Sr_{0.985}Ca_{0.015}TiO_3$ revealed by systematic Nb doping. *npj Quantum Mater.* **7**, 111 (2022).
13. Müller, K. A. & Burkard, H. $SrTiO_3$: an intrinsic quantum paraelectric below 4 K. *Phys. Rev. B* **19**, 3593 (1979).
14. Yamada, Y. & Shirane, G. Neutron scattering and nature of the soft optical phonon in $SrTiO_3$. *J. Phys. Soc. Jpn.* **26**, 396 (1969).
15. Courtens, E. et al. Phonon anomalies in $SrTiO_3$ in the quantum paraelectric regime. *Phys. Scr.* **T49B**, 430 (1993).
16. He, X. et al. Anharmonic eigenvectors and acoustic phonon disappearance in quantum paraelectric $SrTiO_3$. *Phys. Rev. Lett.* **124**, 145901 (2020).
17. Fauqué, B. et al. Mesoscopic fluctuating domains in strontium titanate. *Phys. Rev. B* **106**, L140301 (2022).
18. van der Marel, D., Barantani, F. & Rischau, C. W. Possible mechanism for superconductivity in doped $SrTiO_3$. *Phys. Rev. Res.* **1**, 013003 (2019).
19. Kiselov, D. E. & Feigel'man, M. V. Theory of superconductivity due to Ngai's mechanism in lightly doped $SrTiO_3$. *Phys. Rev. B* **104**, L220506 (2021).
20. Volkov, P. A., Chandra, P. & Coleman, P. Superconductivity from energy fluctuations in dilute quantum critical polar metals. *Nat. Commun.* **13**, 4599 (2022).
21. Yu, Y., Hwang, H. Y., Raghu, S. & Chung, S. B. Theory of superconductivity in doped quantum paraelectrics. *npj Quantum Mater.* **7**, 63 (2022).
22. Gastiasoro, M. N., Temperini, M. E., Barone, P. & Lorenzana, J. Theory of superconductivity mediated by Rashba coupling in incipient ferroelectrics. *Phys. Rev. B* **105**, 224503 (2022).
23. Vugmeister, B. E. & Glinchuk, M. D. Dipole glass and ferroelectricity in random-site electric dipole systems. *Rev. Mod. Phys.* **62**, 993 (1990).
24. Samara, G. A. The relaxational properties of compositionally disordered ABO3perovskites. *J. Phys. Condens. Matter* **15**, R367 (2003).
25. Guzmán-Verri, G. G., Liang, C. H. & Littlewood, P. B. Lamellar fluctuations melt ferroelectricity. *Phys. Rev. Lett.* **131**, 046801 (2023).
26. Setty, C., Baggioli, M. & Zaccone, A. Superconducting dome in ferroelectric-type materials from soft mode instability. *Phys. Rev. B* **105**, L020506 (2022).
27. Setty, C., Baggioli, M. & Zaccone, A. Erratum: superconducting dome in ferroelectric-type materials from soft mode instability [phys. rev. b 105, 020506 (2022)]. *Phys. Rev. B* **106**, 139903 (2022).
28. Rischau, C. W. et al. Isotope tuning of the superconducting dome of strontium titanate. *Phys. Rev. Res.* **4**, 013019 (2022).
29. Devreese, J. T., Klimin, S. N., van Mechelen, J. L. M. & van der Marel, D. Many-body large polaron optical conductivity in $SrTi_{1-x}Nb_xO_3$. *Phys. Rev. B* **81**, 125119 (2010).
30. Bäuerle, D., Wagner, D., Wöhlecke, M., Dorner, B. & Kraxenberger, H. Soft modes in semiconducting SrTiO3: II. The ferroelectric mode. *Z. f.ür. Phys. B Condens. Matter* **38**, 335 (1980).
31. Allen, S. J. et al. Conduction-band edge and Shubnikov–de Haas effect in low-electron-density $SrTiO_3$. *Phys. Rev. B* **88**, 045114 (2013).
32. Fauqué, B. et al. Electronic band sculpted by oxygen vacancies and indispensable for dilute superconductivity. *Phys. Rev. Res.* **5**, 033080 (2023).
33. Lin, X. et al. Critical doping for the onset of a two-band superconducting ground state in $SrTiO_{3-\delta}$. *Phys. Rev. Lett.* **112**, 207002 (2014).
34. Collignon, C. et al. Superfluid density and carrier concentration across a superconducting dome: the case of strontium titanate. *Phys. Rev. B* **96**, 224506 (2017).
35. Thiemann, M. et al. Single-Gap superconductivity and dome of superfluid density in Nb-Doped $SrTiO_3$. *Phys. Rev. Lett.* **120**, 237002 (2018).
36. Edge, J. M., Kedem, Y., Aschauer, U., Spaldin, N. A. & Balatsky, A. V. Quantum critical origin of the superconducting dome in $SrTiO_3$. *Phys. Rev. Lett.* **115**, 247002 (2015).
37. Rowley, S. E. et al. Ferroelectric quantum criticality. *Nat. Phys.* **10**, 367 (2014).
38. Enderlein, C. et al. Superconductivity mediated by polar modes in ferroelectric metals. *Nat. Commun.* **11**, 4852 (2020).
39. Klein, A., Kozii, V., Ruhman, J. & Fernandes, R. M. Theory of criticality for quantum ferroelectric metals. *Phys. Rev. B* **107**, 165110 (2023).
40. Saha, S. K., Gastiasoro, M. N., Ruhman, J. & Klein, A. Strong coupling theory of superconductivity and ferroelectric quantum criticality in metallic srtio$_3$. (2024), arXiv:2412.05374 [cond-mat.str-el].
41. Uwe, H., Yoshizaki, R., Sakudo, T., Izumi, A. & Uzumaki, T. Conduction band structure of $SrTiO_3$. *Jpn. J. Appl. Phys.* **24**, 335 (1985).
42. Martelli, V., Jiménez, J. L., Continentino, M., Baggio-Saitovitch, E. & Behnia, K. Thermal transport and phonon hydrodynamics in strontium titanate. *Phys. Rev. Lett.* **120**, 125901 (2018).
43. Collignon, C. et al. Quasi-isotropic orbital magnetoresistance in lightly doped $SrTiO_3$. *Phys. Rev. Mater.* **5**, 065002 (2021).
44. Lin, X., Fauqué, B. & Behnia, K. Scalable T^2 resistivity in a small single-component Fermi surface. *Science* **349**, 945 (2015).
45. Kumar, A., Yudson, V. I. & Maslov, D. L. Quasiparticle and non-quasiparticle transport in doped quantum paraelectrics. *Phys. Rev. Lett.* **126**, 076601 (2021).
46. Rischau, C. W. et al. A ferroelectric quantum phase transition inside the superconducting dome of $Sr_{1-x}Ca_xTiO_{3-d}$. *Nat. Phys.* **13**, 643 (2017).
47. Hameed, S. et al. Enhanced superconductivity and ferroelectric quantum criticality in plastically deformed strontium titanate. *Nat. Mater.* **21**, 54 (2022).
48. Stuhr, U. et al. The thermal triple-axis-spectrometer eiger at the continuous spallation source sinq. *Nucl. Instrum. Methods Phys. Res. Sect. A Accel. Spectrom. Detect. Assoc. Equip.* **853**, 16 (2017).
49. Piovano, A. & Ivanov, A. The TAS-IN8 upgrade: towards the limit of a three-axis spectrometer performance. *EPJ Web Conf.* **286**, 03011 (2023).
50. Semadeni, F., Roessli, B. & Böni, P. Three-axis spectroscopy with remanent benders. *Phys. B Condens. Matter* **297**, 152 (2001).

Acknowledgements

We thank M. Feigelman, R. Fernandes, D. Kiseliov, M. Gastiasoro, G. Guzmán-Verri, R. Lobo, P. Littlewood, A. Subedi and D. Van Der Marel for useful discussions. This work was supported by the Agence Nationale de la Recherche (ANR-18-CE92-0020-01, ANR-22-CE30-0032-02), by Jeunes Equipes de l'Institut de Physique du Collège de France and by a grant attributed by the Ile de France regional council. This work is based on experiments performed at the Swiss spallation neutron source SINQ, Paul Scherrer Institute, Villigen, Switzerland. This work was also supported by Japan Society for the Promotion of Science (JSPS) KAKENHI Grant Number 23H01135.

Author contributions

La doped samples have been grown by Y.T. Sample alignments have been done by B.F., C.R., and B.B. Electrical transport measurements have been done by S.J. and B.F. Inelastic neutron scattering measurement have been done by B.F., P.B., T.F., B.R., and A.I. Data analysis have been done by B.F. Manuscript has been written by B.F. and K.B.

Competing interests
The authors declare no competing interests.

Additional information
Supplementary information The online version contains supplementary material available at https://doi.org/10.1038/s41467-025-56806-w.

Correspondence and requests for materials should be addressed to Benoît Fauqué.

Peer review information *Nature Communications* thanks the anonymous reviewers for their contribution to the peer review of this work. A peer review file is available.